



Article

Validating Landsat Analysis Ready Data for Nearshore Sea Surface Temperature Monitoring in the Northeast Pacific

Alena Wachmann ^{1,*}, Samuel Starko ^{2,3} , Christopher J. Neufeld ^{2,4} and Maycira Costa ¹¹ Department of Geography, University of Victoria, Victoria, BC V8P 5C2, Canada² Bamfield Marine Science Center, Bamfield, BC V0R 1B0, Canada³ Oceans Institute & School of Biological Sciences, University of Western Australia, Perth, WA 6009, Australia⁴ Department of Biology, University of British Columbia Okanagan, Kelowna, BC V1V 1V7, Canada

* Correspondence: awachmann@uvic.ca

Abstract: In the face of global ocean warming, monitoring essential climate variables from space is necessary for understanding regional trends in ocean dynamics and their subsequent impacts on ecosystem health. Analysis Ready Data (ARD), being preprocessed satellite-derived products such as Sea Surface Temperature (SST), allow for easy synoptic analysis of temperature conditions given the consideration of regional biases within a dynamic range. This is especially true for SST retrieval in thermally complex coastal zones. In this study, we assessed the accuracy of 30 m resolution Landsat ARD Surface Temperature products to measure nearshore SST, derived from Landsat 8 TIRS, Landsat 7 ETM+, and Landsat 5 TM thermal bands over a 37-year period (1984–2021). We used in situ lighthouse and buoy matchup data provided by Fisheries and Oceans Canada (DFO). Excellent agreement (R^2 of 0.94) was found between Landsat and spring/summer in situ SST at the farshore buoy site (>10 km from the coast), with a Landsat mean bias (root mean square error) of 0.12 °C (0.95 °C) and a general pattern of SST underestimation by Landsat 5 of −0.28 °C (0.96 °C) and overestimation by Landsat 8 of 0.65 °C (0.98 °C). Spring/summer nearshore matchups revealed the best Landsat mean bias (root mean square error) of −0.57 °C (1.75 °C) at 90–180 m from the coast for ocean temperatures between 5 °C and 25 °C. Overall, the nearshore image sampling distance recommended in this manuscript seeks to capture true SST as close as possible to the coastal margin—and the critical habitats of interest—while minimizing the impacts of pixel mixing and adjacent land emissivity on satellite-derived SST.

Keywords: Landsat; Analysis Ready Data; nearshore; sea surface temperature (SST); coastal ecosystems



Citation: Wachmann, A.; Starko, S.; Neufeld, C.J.; Costa, M. Validating Landsat Analysis Ready Data for Nearshore Sea Surface Temperature Monitoring in the Northeast Pacific. *Remote Sens.* **2024**, *16*, 920. <https://doi.org/10.3390/rs16050920>

Academic Editors: María Elena Buemi, Nelson Monzón López and Luis Gómez Déniz

Received: 13 February 2024

Revised: 29 February 2024

Accepted: 4 March 2024

Published: 6 March 2024



Copyright: © 2024 by the authors. Licensee MDPI, Basel, Switzerland. This article is an open access article distributed under the terms and conditions of the Creative Commons Attribution (CC BY) license (<https://creativecommons.org/licenses/by/4.0/>).

1. Introduction

Sea surface temperature (SST) is recognized as an essential climate variable that plays a critical role in the health and function of marine ecosystems [1]. As such, significant efforts have gone into establishing SST monitoring programs, e.g., in [2,3], that allow for time-series analysis of seasonal and interannual variability [1]. Traditional methods for monitoring SST include in situ sampling from ships, e.g., [2,3], buoys, and lighthouses [4]. These methods provide ground truth data for the temporal analysis of SST at specific locations. However, they do not provide information on SST dynamics over continuous spatial scales, which vary regionally depending on geographical constraints (i.e., bathymetry, exposure to wind and wave action, currents) [1,2]. This is especially pertinent to nearshore coastal environments, where SST can vary significantly across fine spatial scales [5–8] and have dire implications to coastal ecosystems [9]. Thus, nearshore regions require monitoring systems capable of resolving high spatial and temporal variability [8]. Satellite-retrieved SST can help meet these requirements by providing a synoptic complement to in situ sampling [6]. However, to effectively leverage satellite-derived SST products, it is essential that users evaluate the regional accuracy and precision of satellite SST retrievals [8–11].

Since the 1970s, Earth observation satellites with thermal infrared (TIR) sensors, generally operating at 3.7–12 μm wavelengths, have provided extensive SST data globally [5]. Early spaceborne sensors often acquired TIR data at spatial resolutions > 1 km, limiting their effectiveness for nearshore SST retrieval [6,8]. TIR sensors have since been refined to capture higher spatial resolution TIR (<150 m) [5], improving their ability to measure SST along complex coastlines [8]. The top-of-atmosphere (TOA) TIR radiance (Level-1) measured by a spaceborne sensor is a function of the surface emission, atmospheric path radiance, and atmospheric downwelling irradiance reflected by the Earth's surface and attenuated by the atmosphere [5,10]. Surface emission depends on the temperature and emissivity of the surface [5,10]. For retrieval of SST/land surface temperature (LST), correcting for atmospheric attenuation and accounting for surface emissivity is a fundamental requirement [5,10], thus requiring end-users to have skill sets in image processing. To facilitate the use of these products, there has been a recent surge in Level-2 operational thermal products, such as Analysis Ready Data (ARD) [11,12], to improve the accessibility of high-fidelity satellite-derived surface temperature data to a broader demographic [5,8,11]. ARD and similar science-grade products provide geometrically and radiometrically consistent observations based on standardized calibration methodologies for the streamlined analysis of temperature trends [10,11].

However, uncertainties introduced into satellite-derived SST associated with adjacent land emissivity and pixel mixing at the land–water boundary must be considered [5,6,8,13–16]. Land adjacency refers to the effects of TIR scattering from land pixels into the field of view of adjoining water pixels [6,14,16]. Pixel mixing is the result of having multiple surface types (e.g., land and water) captured within a single-image pixel, a function of the satellite's spatial resolution and the complexity of the geography being observed [17]. Both are common limitations of accurate nearshore SST retrieval from satellite imagery [8], requiring specific parameters for the selection of pixels most representative of true nearshore SST. Temperature data for nearshore ecosystems can enhance our understanding of thermal stress conditions associated with climate change and marine heatwaves [18]. This information is valuable for guiding various restoration and management initiatives including the monitoring of temperature tolerances for coral, eelgrass, kelp, and fisheries [9,17–24].

Here, we evaluated the accuracy of SST retrieval from Landsat 8 TIRS, Landsat 7 ETM+, and Landsat 5 TM ARD Surface Temperature products, with minimal additional processing, for nearshore waters on the west coast of Canada. This was accomplished by comparing satellite-derived SST against in situ SST observations from 1984 to 2021 at four sites in the Salish Sea, BC, representing various coastal dynamic conditions. Specifically, data were analyzed at (i) farshore (>10 km from the coast) and (ii) nearshore (<360 m from the coast) sites to consider the impacts of distance from the shore, season, sensor, and water column mixing conditions on Landsat SST retrieval with reference to in situ SST. From that, we define the best general conditions and considerations for the application of Landsat ARD SST for monitoring nearshore regions.

2. Materials

2.1. Study Area

Located along the southern region of Canada's Pacific coast (Figure 1), the Salish Sea (48.3295°N , 123.1407°W) is a marginal sea characterized by interannual variability in SST due to large-scale oceanographic drivers, such as the Pacific Decadal Oscillation (PDO) and the El Niño–Southern Oscillation (ENSO) and freshwater river inputs [25]. Tides, currents, and winds also cause diurnal and seasonal SST variability that is highly localized [7,26]. This mid-latitude temperate region experiences balanced winters and summers, with SSTs ranging from approximately 4.0°C to 23.0°C [7,27]. Spatially, this region shows a general SST gradient of cold water from the open ocean on the southwest coast of Vancouver Island, through the Juan de Fuca Strait and Haro Strait, into generally warmer conditions in the Strait of Georgia, which is accentuated during the summer [25,27,28]. Temporally, SST in

the Salish Sea has increased between 0.7 °C and 2.2 °C from 1935 to 2014 [7], with present models predicting an average SST increase of about 1.5 °C by 2095 [29].

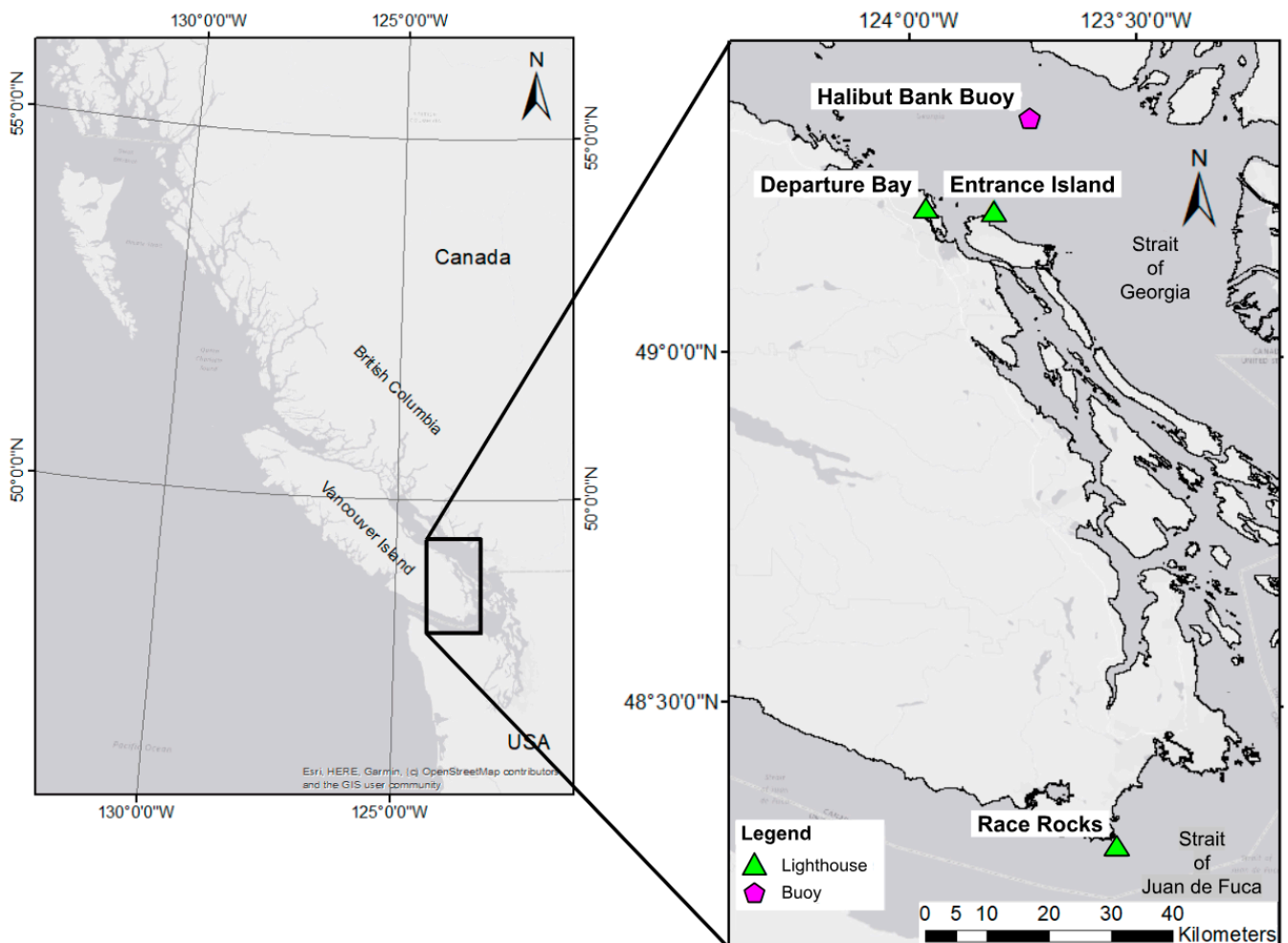


Figure 1. Map of the Salish Sea study area (48.3295°N, 123.1407°W), a marginal sea off the coast of British Columbia, Canada, in the Northeast Pacific. In situ sampling locations (lighthouse = green triangle; buoy = pink pentagon) around Southern Vancouver Island are included.

To capture the varying thermal regimes and diverse geographies of this region [30,31], the four monitoring stations presented in Table 1 were chosen for this study, with geographic locations presented in Figure 1. For the lighthouse stations, fetch was used to represent the gradient of exposure experienced at each site (Canada Open Data: <https://open.canada.ca/data/en/dataset/412431c4-7363-410e-86a4-76feb9a6dcde> (accessed on 15 June 2023)). The sum fetch (m), calculated by summing the distance in meters to the nearest land mass at every 5-degree bearing around a point on the shoreline, is described for the nearest point to the sample site.

Table 1. In situ SST site information.

Site Name	Location	Adjacent to Coast?	Temporal Resolution	Description
Halibut Bank buoy	49°20'24"N, 123°43'48"W	No	Hourly	Operated by Environment and Climate Change Canada, this buoy is located about 10.7 km offshore in the central Strait of Georgia (Figure 1) and has been used in the past to validate other satellite SST products [5]. Seasonally, the SST ranges from 4.2 °C to 22.0 °C [32].
Race Rocks lighthouse	48°17'54"N, 123°31'54"W	Yes	Daily	Located on an island at the southern tip of Vancouver Island (Figure 1), this lighthouse station experiences the most stable SSTs year-round (5.9–13.3 °C) [32] due to consistent upwelling of deep water along the west coast of Vancouver Island and strong currents and wind–wave action (fetch = 989,674 m) from the Strait of Juan de Fuca [30].
Entrance Island lighthouse	49°12'33"N, 123°48'29"W	Yes	Daily	This is a moderately exposed (fetch = 686,219 m) lighthouse located midway into the Salish Sea, Vancouver Island (Figure 1). This lighthouse undergoes strong seasonal variation in SST (5.8–22.8 °C) [32] and wave action from the Strait of Georgia [31].
Departure Bay lighthouse	49°12'39"N, 123°57'20"W	Yes	Daily	The most sheltered (fetch = 32,093 m) of the lighthouse stations, Departure Bay undergoes strong seasonal variation in SST (6.1–22.5 °C) because of limited tide mixing and strong influences from nearby freshwater outfalls [7]. This station is located on the north side of Nanaimo Harbour (Figure 1), protected by the Brandon Islands, and presents the most complex geography among the selected sites.

2.2. Datasets

2.2.1. In Situ SST Data

Generally, measured in situ SST is a function of the measurement technique, sensor characteristics, depth within the water column, local heat flux conditions at the air–water interface, and time of day the measurement was obtained [33,34]. In this study, both farshore and nearshore in situ SST are representative of bulk subsurface temperatures (~1 m) within the upper mixed layer, where turbulent heat transfer processes dominate [34]. In comparison, satellite radiometers measure thermal radiance from the top microns (~10–20 µm) of the water surface [10], also known as skin temperature, where conductive and diffusive heat transfer processes generally result in cooling at the water side of the air–sea interface [33,34].

(i) Farshore In Situ Site (Halibut Bank Buoy)

For the Halibut Bank buoy (established in 1992), we obtained hourly water temperature data (in °C) measured by the sensor at ~1 m depth (Tz), as well as horizontal wind speed data (in meters/second at 5 m above the surface). These data were sourced from the Marine Environmental Data Section Archive [35,36] (<https://meds-sdmm.dfo-mpo.gc.ca/isdm-gdsi/waves-vagues/data-donnees/data-donnees-eng.asp?medsid=C46146> (accessed on 19 November 2021)). To facilitate comparison with corresponding Landsat images, which are captured at noon local time (within +/-20 min), we isolated the nearest water tempera-

ture observation to noon (± 1 h) for matchup. This approach also enabled us to compare farshore and nearshore matchup results, as in situ sampling at the lighthouses is only conducted during daylight hours. Additionally, farshore in situ SST measurements were modified to skin temperature [12,33,34,37], by applying a subsurface-to-skin temperature adjustment [12,34], adapted from Zeng et al. [38], as the following:

$$a = 0.05 - \frac{0.6}{w} + 0.03\ln(w) \quad (1)$$

$$T_s = T_z - az - d \quad (2)$$

The thermal gradient (a) was calculated based on the 24 h average wind speed measured at the buoy (w). Hourly wind speed data (m/s) was averaged for the 24 h prior to satellite overpass (w). Low wind conditions (24 h average < 1 m/s) were removed due to little mixing between subsurface and near-surface waters, causing poor correlation between the temperatures [12]. Next, this gradient was incorporated to adjust the subsurface temperature (T_z) observed by the buoy in $^{\circ}\text{C}$ at depth z (in meters) to the bulk subsurface temperature ($T_z - az$). Finally, the bulk subsurface was adjusted to skin temperature (T_s) using a constant d (0.17 $^{\circ}\text{C}$), from Donlon et al. [33], as an approximate for the surface cool skin effect under a range of clear sky conditions. T_s is hereafter called $\text{SST}_{\text{in situ}}$.

(ii) Nearshore In Situ Sites (BC Lighthouse Stations)

Daily mean ST measurements are recorded at lighthouse stations (British Columbia Shore Station Oceanographic Program) using the “bucket method”, whereby observations are made from seawater collected by lowering a bucket into surface waters at or near daytime high tide (6 a.m.–6 p.m. LST) [32]. Archived SST data were downloaded from the DFO data server (<https://open.canada.ca/data/en/dataset/719955f2-bf8e-44f7-bc26-6bd623e82884> (accessed on 19 November 2021)). For each site, information on the location of in situ SST sampling (Figure 2) was considered based on illustrative maps provided by DFO (pers. comm., [36]) and occurs specifically as the following:

- (1) Race Rocks—off the dock at the northwest side of the island;
- (2) Entrance Island—off the dock on the island’s south side;
- (3) Departure Bay—off the dock to the southwest of the Pacific Biological Station.

No additional adjustments were made to the nearshore SST ($^{\circ}\text{C}$), also referred to as the $\text{SST}_{\text{in situ}}$, due to the sufficient mixing of surface waters (< 1 m) during “bucket method” retrieval.

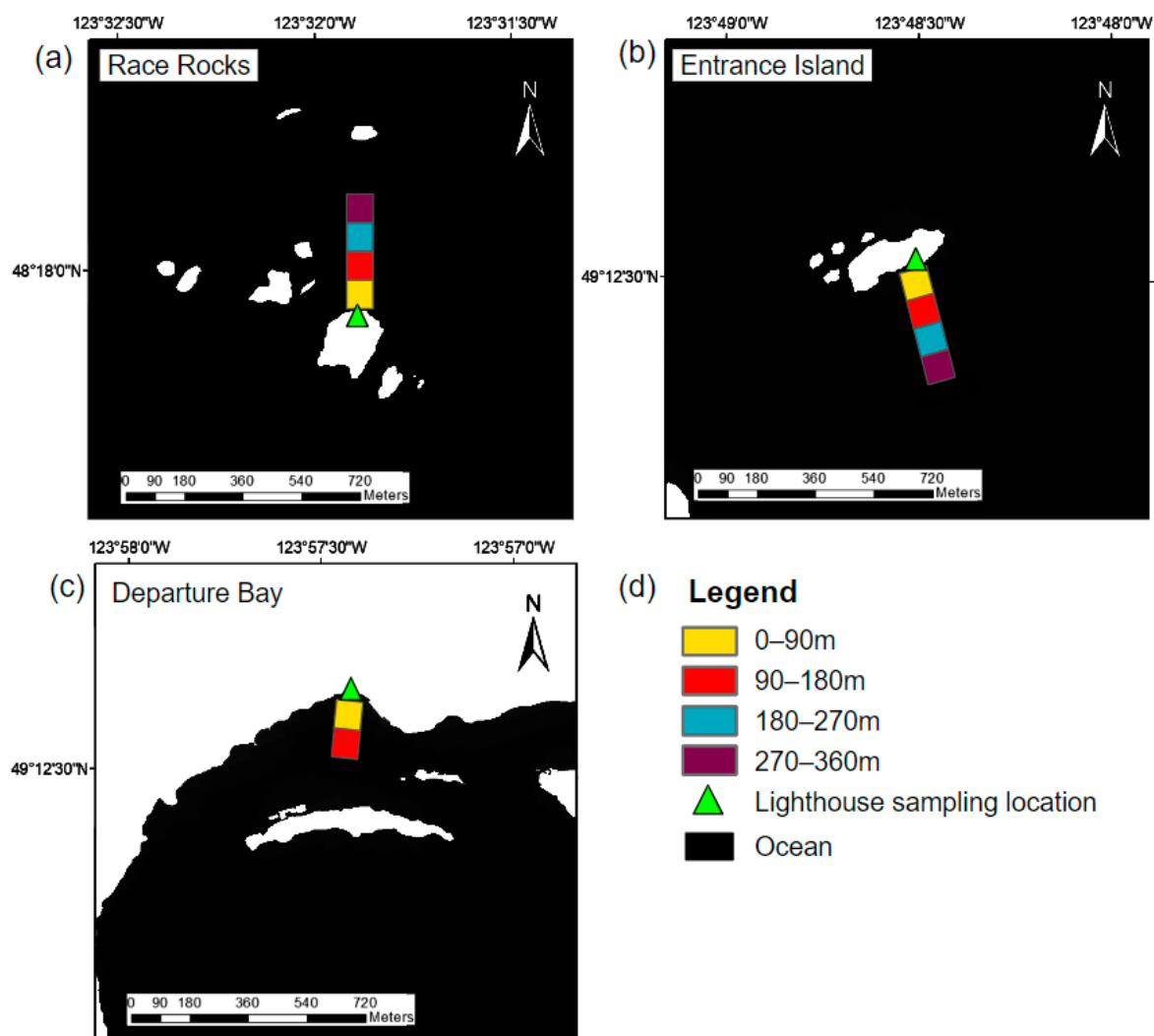


Figure 2. Sampling polygons at incremental distances from the coast used to extract SST_{Lsat} at lighthouse locations—(a) Race Rocks, (b) Entrance Island, and (c) Departure Bay. Legend is shown in (d). A Canadian Hydrographic Service (CHS) Low Water Mark (LWM) was used as a land mask (white area).

2.2.2. Landsat ARD ST Images

For this study, Level-2 ST products, part of the Landsat ARD suite, were utilized with limited additional processing to assess their accuracy for direct application by end-users. The 30 m resolution ARD products come atmospherically corrected, tiled, geometrically corrected, and defined in an equal-area projection [11,16,39]. For ST product generation, thermal data from Landsat TM (120 m), ETM+ (60 m), and TIRS (100 m) were resampled to 30 m using a cubic convolution resampling algorithm [10]. ARD ST products were calculated by applying a single-channel algorithm [40], developed by Cook et al. [12] and later refined by Malakar et al. [10], on TIRS Band 10 (10.6–11.2 μm) and TM/ETM+ Band 6 (10.4–12.5 μm), generated from the Landsat Level-2 Surface Temperature algorithm version 1.3.0. (derived from the June 2017 version of RIT ST code) [11]. This algorithm includes several auxiliary data inputs for calibration: (i) the North America Regional Reanalysis (NARR) data from the National Centers for Environmental Prediction (NCEP) to characterize the atmosphere (air pressure, temperature, and relative humidity) alongside; (ii) the MODTRAN 5.2 radiative transfer code [39] to calculate atmospheric transmission, upwelling, and downwelling radiances for multiple levels in the atmosphere; and (iii) the Advanced Spaceborne Thermal Emission and Reflection Radiometer Global Emissivity Dataset (ASTER GED) by

the Land Processes Distributed Active Archive Center (LP DAAC) to convert at-surface brightness temperature to surface temperature based on surface emissivity maps [10–12,41]. Links to ARD product development guides can be found through <https://www.usgs.gov/landsat-missions/landsat-collection-2-us-analysis-ready-data> (accessed on 2 September 2021), with detailed data format information available in the Data Format Control Book (https://d9-wret.s3.us-west-2.amazonaws.com/assets/palladium/production/s3fs-public/media/files/LSDS-1435_Landsat-C2_US-ARD_Data-Format-Control-Book-v4.pdf (accessed on 2 September 2021)).

ARD ST images were downloaded from the Collection 2 archive (<https://earthexplorer.usgs.gov> (accessed on 2 September 2021)) according to the following criteria: (i) image coverage coinciding with in situ sampling sites and (ii) cloud cover threshold of <10% [6]. The initial search resulted in 1505 images, which were pared down to 351 after visual assessment using the corresponding Pixel Quality Assessment (PIXELQA) layer [6,10,41]. Landsat 7 ETM+ images acquired after 31 May 2003 were removed due to the poor quality associated with the malfunction of the Scan Line Corrector [42]. Images were also excluded if cloud contamination was assessed within 500 m of the in situ site location. Overall, our final dataset of 351 images consisted of 76 acquired by Landsat 8 TIRS, 38 by Landsat 7 ETM+, and 237 by Landsat 5 TM, covering the entire time series (4 to 19 images per year from 1984 to 2021, except for 2012 due to a lack of matchups).

The selected images represented the surface temperature in Kelvin following the application of Landsat-defined conversion coefficients ($K = DN \times 0.00341802 + 149$) [11]. Image values were then converted to degrees Celsius ($^{\circ}C = K - 273.15$), hereafter called SST_{Lsat} , for ease of comparison with the $SST_{in\ situ}$. Next, the images were organized according to the (1) sensor (Landsat 5, 7, and 8), (2) site overlap, and (3) season. Images were categorized into two seasons (winter = $\alpha \leq 30^{\circ}$ and spring/summer = $\alpha > 30^{\circ}$) based on the local noon solar elevation angle (α), accessed from the National Oceanic and Atmospheric Administration (NOAA)'s online Solar Geometry Calculator (<https://gml.noaa.gov/grad/antuv/SolarCalc.jsp> (accessed on 11 October 2021)). Under this method, 7% of usable images (23 of 351) were classified as winter, and 93% (328 of 351) were classified as spring/summer.

3. Methods

The SST_{Lsat} validation considered the following data scenarios:

- (i) At the farshore buoy location (Figure 1), an 8100 m² polygon (Landsat ARD 3 × 3 pixel window) centred over the site was used to extract image zonal statistics of mean and standard deviation SST_{Lsat} for matchup comparison with corresponding $SST_{in\ situ}$ buoy observations. Matchups were removed if the standard deviation was >2.0 °C within the pixel window to limit errors associated with surface heterogeneity [10,41,43].
- (ii) For the three nearshore locations, a Canadian Hydrographic Service (CHS) Low Water Mark (LWM) (<https://catalogue.data.gov.bc.ca/dataset/chs-low-water-mark-lines> (accessed on 1 September 2021)) was used to delineate the coastline around the lighthouse locations (Figure 1). From the derived coastline, a 3 × 12 pixel transect was defined as perpendicular to the coast from the local dock where $SST_{in\ situ}$ was collected (Figure 2). Each transect was then subdivided into four distance groups covering nine (3 × 3) pixels each: 0–90 m, 90–180 m, 180–270 m, and 270–360 m. For the Departure Bay lighthouse site, sampling was not possible past 180 m from the coast because a small island offshore from the lighthouse created a geographical constraint (Figure 2c). The mean SST_{Lsat} value and standard deviation of each 3 × 3 pixel window were extracted for each data analysis scenario [10,41,43].

For both the farshore and nearshore, a linear regression relationship between $SST_{in\ situ}$ and SST_{Lsat} , and mean bias (°C; MB), mean relative bias (%; MRB), root mean square error

(°C; RMSE), and proportional root mean square error (%; pRMSE) were used to evaluate retrieved SST_{Lsat} [6,10,41,43,44].

$$MB = \frac{1}{N} \times \sum (SST_{Lsat} - SST_{in situ}) \quad (3)$$

$$MRB = 100 \times \frac{1}{N} \times \sum \left(\frac{SST_{Lsat} - SST_{in situ}}{SST_{in situ}} \right) \quad (4)$$

$$RMSE = \sqrt{\frac{1}{N} \times \sum (SST_{Lsat} - SST_{in situ})^2} \quad (5)$$

$$pRMSE = \sqrt{100 \times \frac{1}{N} \times \sum \left(\frac{SST_{Lsat} - SST_{in situ}}{SST_{in situ}} \right)^2} \quad (6)$$

Evaluations were conducted considering different sample populations based on the site location, Landsat sensor, season, distance from the coastline, and SST range, to isolate conditions that may have impacted the quality of the SST_{Lsat}.

4. Results

4.1. Farshore Results

SST_{in situ} observed at the Halibut Bank buoy were between 4.0 °C and 22.7 °C, thus providing a good range of values to validate the Landsat ARD. Winter temperatures ranged from 4.0 °C to 8.8 °C, while spring/summer temperatures ranged from 6.5 °C to 22.7 °C. A total of 134 images, and therefore data points (Figure 3, Table 2), revealed the high accuracy of the SST_{Lsat} when compared to the SST_{in situ} (MB of 0.03 °C, with an associated pRMSE of 8.39%, and a high R² value of 0.96). For the entire SST_{in situ} dataset, the relationship between the SST_{Lsat} (y) and SST_{in situ} (x) is described by the regression $y = 1.08 \times x + -1.1$, with the largest SST_{Lsat} residual of 3.01 °C from Landsat 5 in 2009. Overall, this population displayed a mean of 0.03 °C, a standard deviation of 0.97 °C, and a 95% confidence interval of biases between -0.14 °C and 0.19 °C.

Of note, the SST_{Lsat} shows an underestimation (-0.46 °C) at the lower temperatures and an overestimation (0.51 °C) at the higher temperatures (Figure 3, Table 2). Furthermore, the pRMSE (%) is greatest at low temperatures (13.76% at <10 °C) and generally decreases as temperatures increase (5.09% at >20 °C). General low temperature underestimation was well captured with the separation of winter from spring/summer matchups (Figure 4, Table 3), where the MBs (pRMSEs) are -0.69 °C (17.07%) and 0.20 °C (6.31%), respectively. Regression results improved across all satellites with the isolation of spring/summer matchups (Figure 4, Table 3), improving the offset from -1.1 °C to -0.82 °C, and slightly improving the slope from 1.08 to 1.06. For datasets from each Landsat satellite (Figure 5, Table 4), the results showed similar relationships for Landsat 5 (L5), 7 (L7), and 8 (L8) across all seasons, with the lowest MB from L5 (-0.28 °C), highest MB from L8 (0.65 °C), and pRMSEs between 9.42% (L5) and 6.17% (L8). R² values varied slightly across satellites but remained very high in all cases (between 0.96 and 0.98).

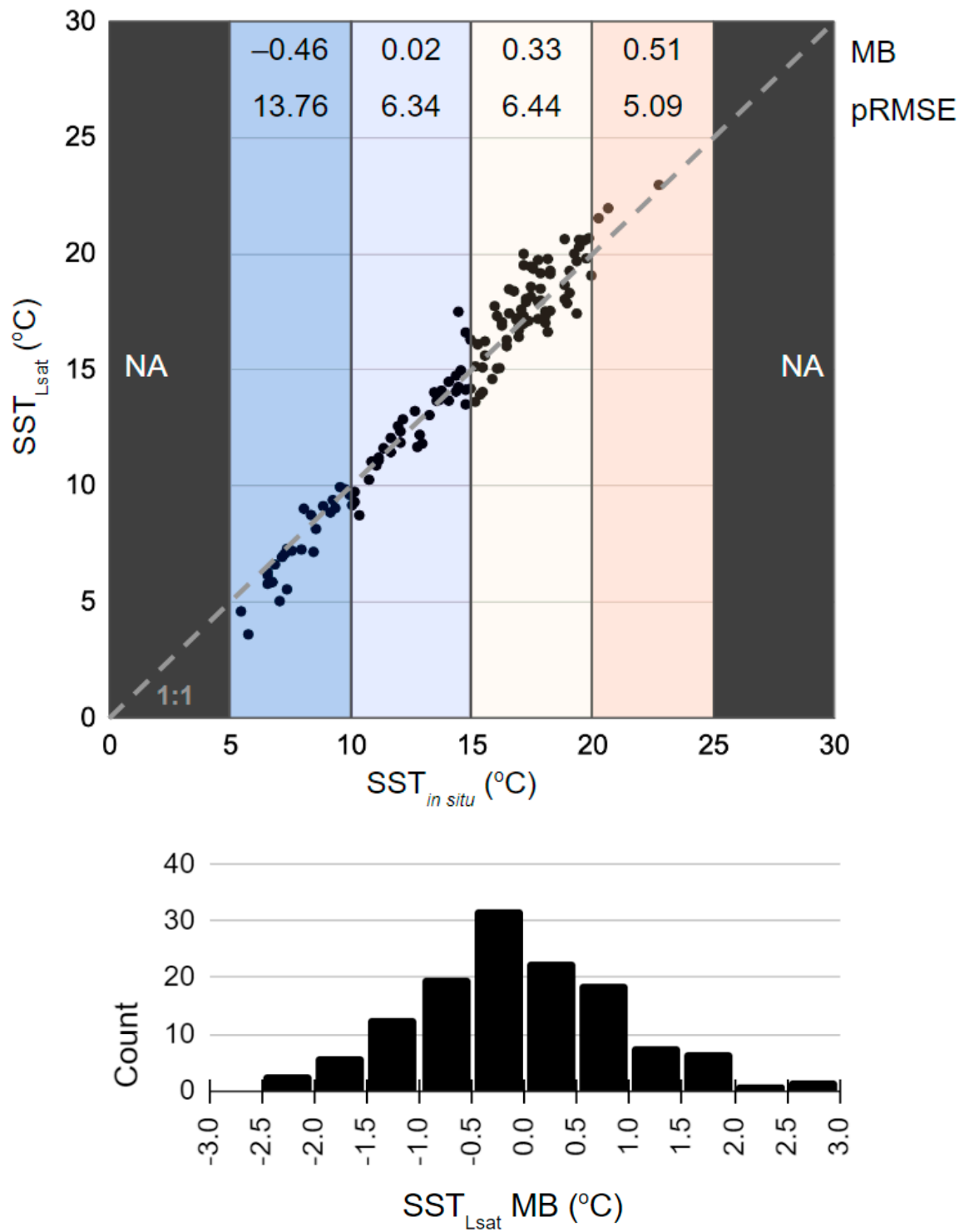
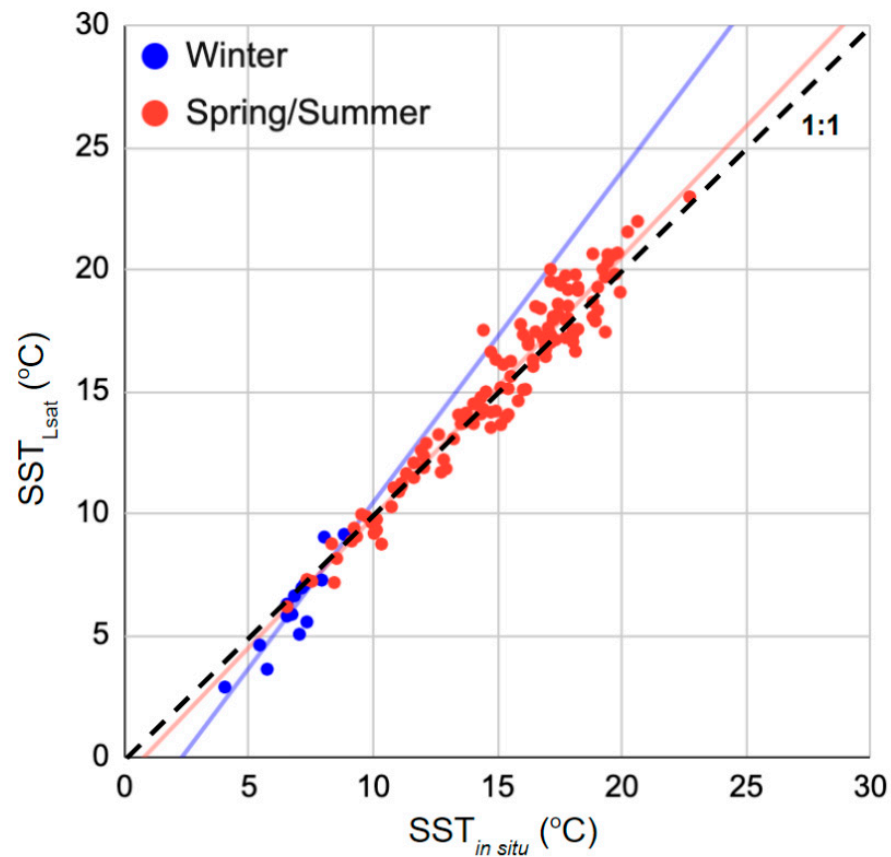


Figure 3. Regression plot of all farshore matchup results, including the MB ($^{\circ}C$) and pRMSE (%) of in situ binned ($5^{\circ}C$) temperature groups (**above**). Frequency distribution of the farshore matchup SST_{Lsat} biases (**below**).

Table 2. Statistical output for farshore SST_{Lsat} matchups for the entire dataset and 5 °C ranges of temperature (Figure 3).

Thermal Range	MB (°C)	MRB (%)	RMSE (°C)	pRMSE (%)	Slope	Offset	R Squared	N
Total	0.03	−0.96	0.97	8.39	1.08	−1.1	0.96	134
<10 °C	−0.46	−7.39	0.88	13.76	N/A	N/A	N/A	25
10–15 °C	0.02	−0.12	0.83	6.34	N/A	N/A	N/A	37
15–20 °C	0.33	1.88	1.10	6.44	N/A	N/A	N/A	68
>20 °C	0.51	2.42	1.04	5.09	N/A	N/A	N/A	4

**Figure 4.** Relationship between farshore match-up Landsat and in situ SST categorized by season, including linear trendlines.**Table 3.** Statistical output for farshore SST_{Lsat} categorized by season (Figure 4).

Season	MB (°C)	MRB (%)	RMSE (°C)	pRMSE (%)	Slope	Offset	R Squared	N
Spring/Summer	0.12	0.38	0.95	6.23	1.06	−0.82	0.94	120
Winter	−0.76	−12.51	1.15	18.51	1.34	−3.52	0.82	14

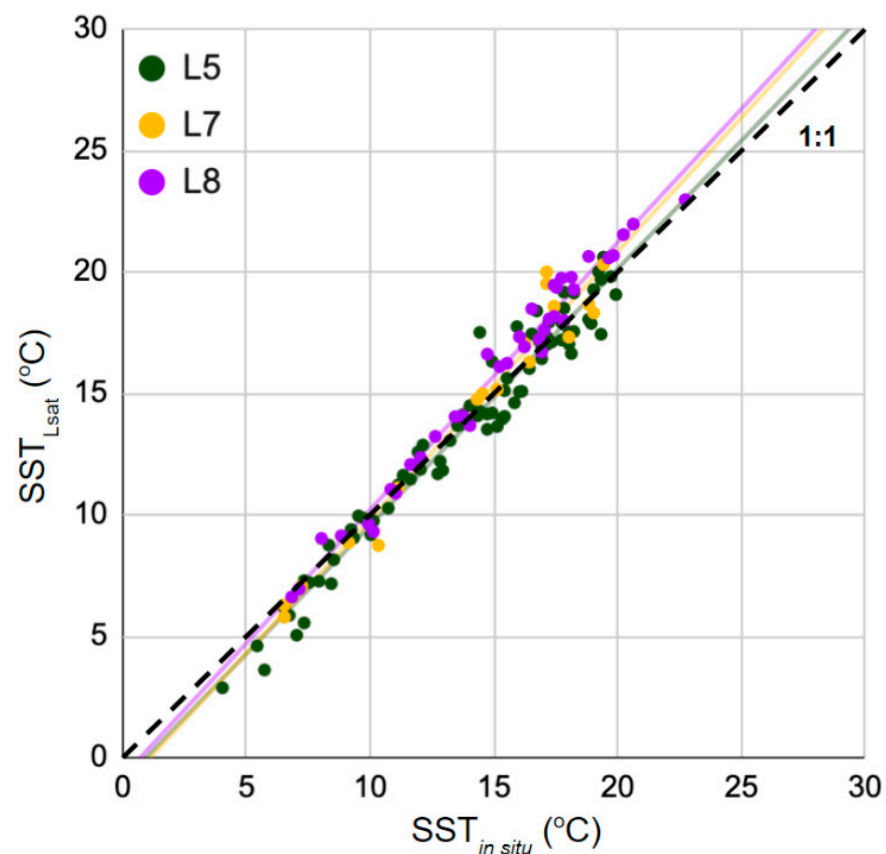


Figure 5. Relationship between farshore match-up Landsat and in situ SST, categorized by satellite, for all seasons, including linear trendlines.

Table 4. Statistical output for farshore SST_{Lsat} matchups, categorized by sensor (Figure 5), where Landsat 5 TM, Landsat 7 ETM+, and Landsat 8 TIRS are represented by L5, L7 and L8, respectively.

Sensor	MB (°C)	MRB (%)	RMSE (°C)	pRMSE (%)	Slope	Offset	R Squared	N
L5	−0.28	−3.28	0.96	9.42	1.05	−1.05	0.96	79
L7	0.1	−0.58	1.05	7.54	1.09	−1.26	0.96	18
L8	0.65	3.79	0.98	6.17	1.09	−0.72	0.98	37

4.2. Nearshore Results

Global analysis of the nearshore sites led to 512 matchups each for the 0–90 m and 90–180 m distance groups across all three lighthouse locations along with 334 matchups each for 180–270 m and 270–360 m distance groups from the Race Rocks and Entrance Island sites (Table 5) due to geographic constraints at the Departure Bay site. Winter $SST_{in situ}$ at the nearshore sites ranged from 5.6 °C to 9.3 °C, while spring/summer $SST_{in situ}$ ranged from 6.0 °C to 22.6 °C. Year-round, Race Rocks experienced the lowest and most consistent SST (5.7 °C to 13.1 °C), while Entrance Island and Departure Bay stations experienced a wider range of thermal conditions (5.6 °C to 22.6 °C and 5.9 °C to 22.3 °C, respectively).

SST_{Lsat} from all distance groups produced relatively high R^2 values between 0.87 and 0.91 (Table 5). Generally, SST_{Lsat} directly adjacent to the coast, within the 0–90 m distance group, overestimated $SST_{in situ}$ by an MB (RMSE) of 0.58 °C (1.78 °C) (Figure 6, Table 5). Moving away from the coast, SST_{Lsat} at 90–180 m was lower than $SST_{in situ}$ by an MB (RMSE) of −0.61 °C (1.74 °C). SST_{Lsat} from both 180 to 270 m and 270 to 360 m further underestimated $SST_{in situ}$ by about 1.0 °C.

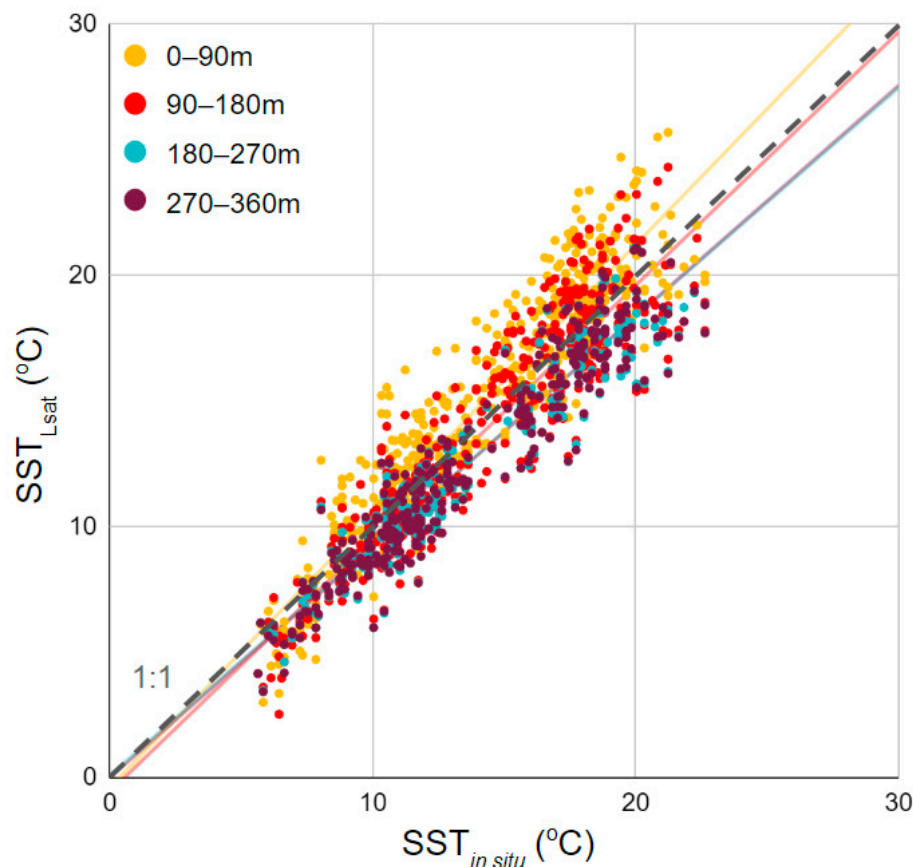


Figure 6. Relationship between nearshore matchup SST_{Lsat} and $SST_{in situ}$ at varying distances from the coastline for all lighthouse sites, including linear trendlines.

Table 5. Statistical output for SST_{Lsat} matchups at varying distances from the coastline (Figure 6). * = no data from Departure Bay.

Distance from Coast	MB (°C)	MRB (%)	RMSE (°C)	pRMSE (%)	Slope	Offset	R Squared	N
0–90 m	0.58	3.35	1.78	13.74	1.08	−0.56	0.88	512
90–180 m	−0.61	−4.98	1.74	12.98	1.01	−0.72	0.87	512
180–270 m *	−1.25	−9.31	1.78	13.12	0.91	0.05	0.91	334
270–360 m *	−1.27	−9.44	1.79	13.28	0.92	0.15	0.91	334

Next, considering only the two distance groups that most closely matched the $SST_{in situ}$ statistically (0–90 m and 90–180 m), seasonal impacts to SST_{Lsat} were investigated by separating data acquired during the winter and spring/summer. We observed similar negative biases at 0–90 m and 90–180 m during the winter (Figure 7, Table 6) of -1.05 °C and -1.10 °C as well as high pRMSE values of 23.75% and 22.35%, respectively. In comparison, the isolation of the spring/summer observations showed a positive MB (RMSE) at 0–90 m of 0.71 °C (12.63%) and improved trendline offsets and slopes for both distances (Figure 7, Table 6). The overall best-performing population (and low variance) from this analysis was the spring/summer matchups at 90–180 m, which produced an MB of -0.57 °C (pRMSE of 11.95%) and an R^2 of 0.83.

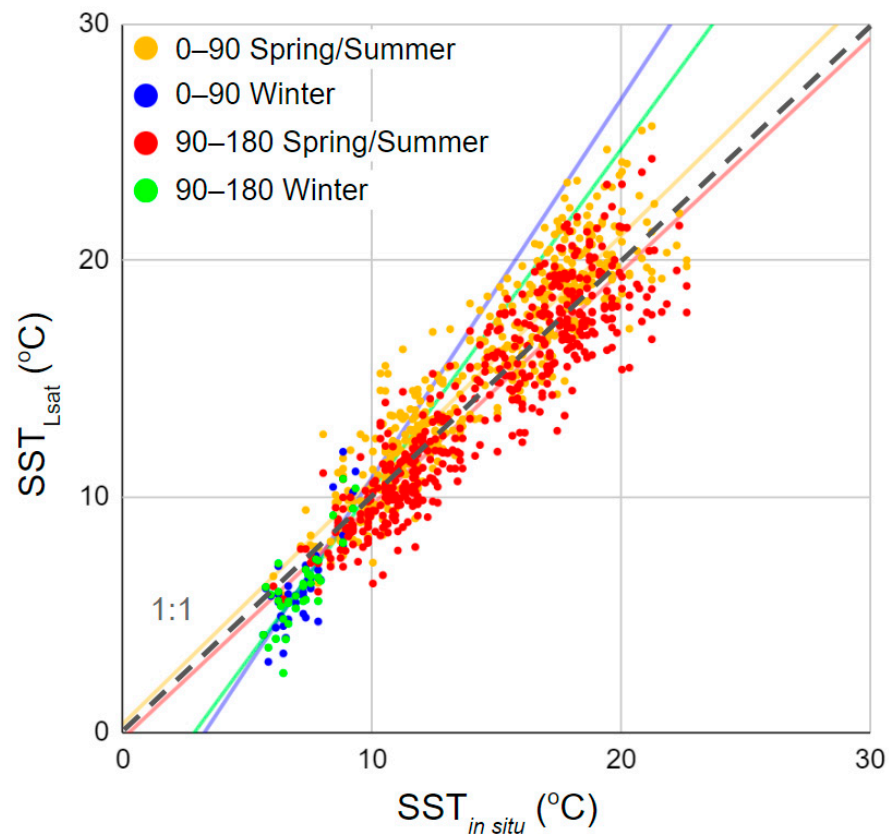


Figure 7. Relationship between nearshore matchups of SST_{Lsat} and $SST_{in\ situ}$ for the <180 m dataset, categorized by season, including linear trendlines.

Table 6. Statistical output for SST_{Lsat} matchups 0–90 m and 90–180 m from the coast, categorized by season (Figure 7).

Distance: Season	MB (°C)	MRB (%)	RMSE (°C)	pRMSE (%)	Slope	Offset	R Squared	N
0–90 m: Spring/Summer	0.71	4.28	1.78	12.63	1.03	0.22	0.85	475
0–90 m: Winter	−1.05	−15.43	1.70	23.75	1.60	−5.49	0.64	37
90–180: Spring/Summer	−0.57	−4.13	1.75	11.95	0.99	−0.39	0.83	475
90–180 m: Winter	−1.1	−15.84	1.55	22.35	1.44	−4.35	0.67	37

Breaking down the spring/summer 90–180 m population by site (Figure 8, Table 7) revealed a positive MB (0.67 °C) at the most protected lighthouse location, Departure Bay (Figure 1), compared to the two more exposed lighthouse locations, Race Rocks and Entrance Island (−0.93 °C and −1.43 °C, respectively). The R^2 was the lowest at Race Rocks (0.46), which also experienced the narrowest range of thermal conditions (7.4 °C versus ~17.0 °C dynamic range at the other two sites).

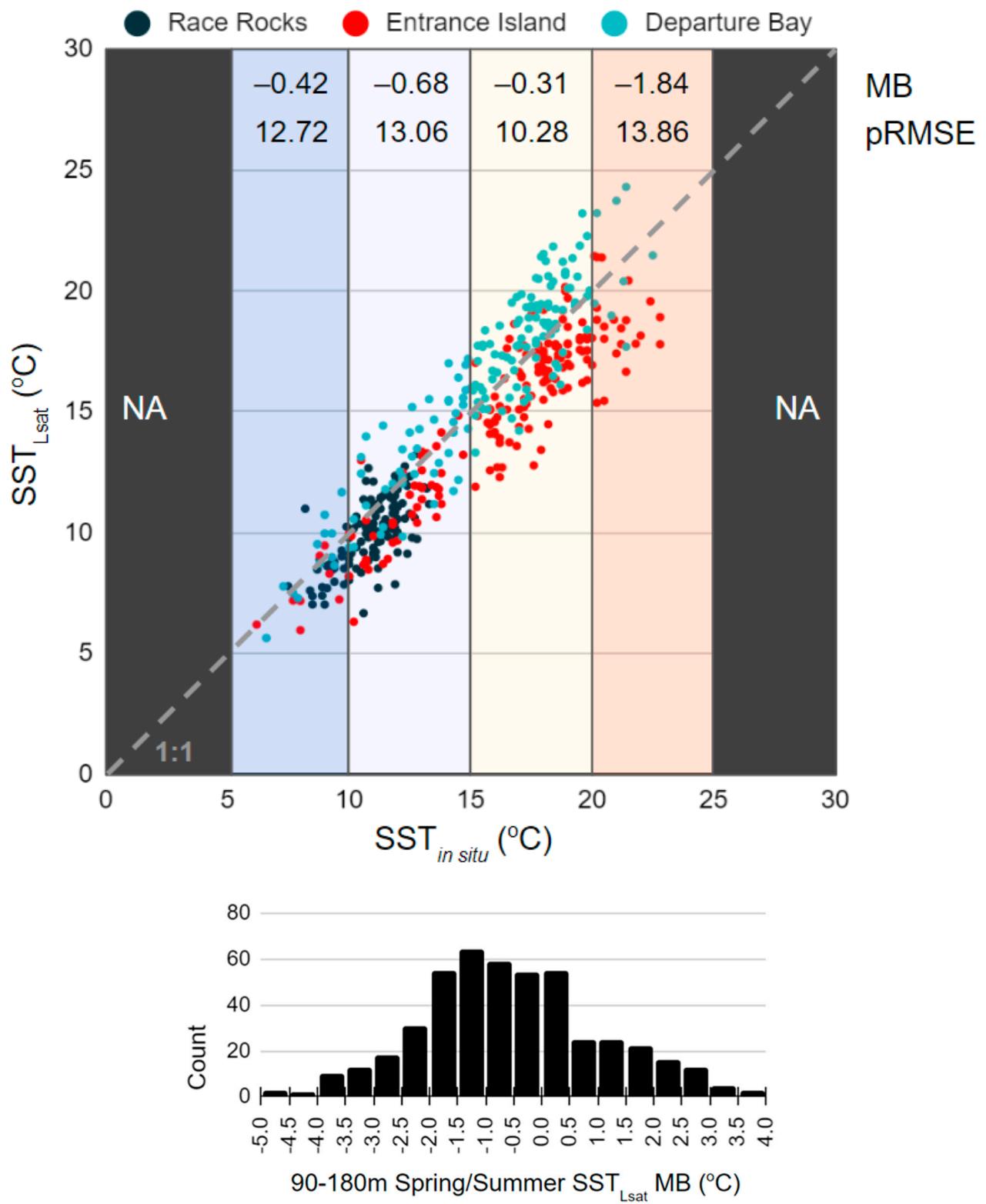


Figure 8. Regression plot of the SST_{Lsat} and SST_{in situ} for spring/summer matchups 90–180 m from the coast, including the MB (°C) and pRMSE (%) of 5 °C binned in situ ranges (above). Points are colour coded by lighthouse site. Frequency distribution of nearshore SST_{Lsat} biases for this population (below).

Table 7. Statistical output for spring/summer matchups 90–180 m from the coast, categorized by site and binned into 5 °C in situ temperature ranges (Figure 8).

90–180 m, Spring/Summer	MB (°C)	MRB (%)	RMSE (°C)	pRMSE (%)	Slope	Offset	R Squared	N
Location								
Race Rocks	−0.93	−8.39	1.41	12.84	0.81	1.14	0.46	127
Entrance Island	−1.43	−8.71	2.03	12.41	0.90	0.16	0.83	183
Departure Bay	0.67	4.23	1.65	10.64	1.03	0.13	0.84	165
Temp. Range								
<10 °C	−0.42	−4.7	1.13	12.72	N/A	N/A	N/A	55
10–15 °C	−0.68	−5.91	1.54	13.06	N/A	N/A	N/A	183
15–20 °C	−0.31	−1.69	1.8	10.28	N/A	N/A	N/A	210
>20 °C	−1.84	−8.63	2.94	13.86	N/A	N/A	N/A	27

Beyond different results among the stations, across temperature ranges (binned 5 °C in situ intervals) (Figure 8, Table 7), the MB remained negative, was the smallest at mid-range temperatures (−0.42 °C at 15.0–20.0 °C), and was the largest at high temperatures (−1.84 °C at >20.0 °C). In addition, the RMSE increased with temperature (1.13 °C at <10.0 °C, to 2.94 °C at >20.0 °C); however, the pRMSE (10.28–13.86%) remained relatively stable across the thermal ranges (Table 7). For spring/summer 90–180 m biases, the histogram in Figure 8 shows a slightly left-skewed (negative MB) distribution, with a peak around −1.00 °C. A Shapiro–Wilk normality test resulted in a *W*-statistic of 0.99216 and a *p*-value of 0.01335, suggesting the data was normally distributed. As such, this population had a mean of −0.57 °C, with a 95% confidence interval between −0.72 °C and −0.42 °C. For this population, the relationship between the SST_{Lsat} (*y*) and SST_{in situ} (*x*) is described by the regression $y = 0.99x + -0.39$, with a largest SST_{Lsat} residual of −5.04 °C observed by Landsat 5 at Entrance Island in September 1993 (Figure 8).

5. Discussion

Matchup analysis between in situ and satellite-derived measurements is generally considered a standard approach for validating satellite products [41,45,46]. However, spatial and temporal differences between in situ and satellite data [47], including errors introduced by in situ sampling methods and satellite sensor calibration, introduce uncertainty [48]. This is especially true for dynamic coastal environments, which are often flagged and removed from analysis [8], but which are extremely valuable regions of study [5,6,19]. As such, the following discussion will review considerations for the use of Landsat ARD for nearshore SST retrieval based on our results, including possible sources of matchup uncertainty, sensor-specific, and calibration algorithm biases.

5.1. Considerations for the Use of LANDSAT ARD for Nearshore SST

This research used a dataset of 646 matchups between 345 images and in situ data to validate SST retrievals from Landsat ARD ST products for nearshore environments in the Northeast Pacific. Landsat 5, 7, and 8 thermal sensors originally acquire data at spatial resolutions of 120 m, 60 m, and 100 m, respectively, with the resampled 30 m ARD pixels representing a temperature value calculated by a cubic convolution interpolation kernel [10,49,50]. Schaeffer et al. [6] showed that, considering resampling [6,10,11] and Landsat's general geolocation uncertainty of <12 m [2], pixel mixing and interference from land pixel thermal radiance into water pixel thermal radiance can occur up to a maximum of 180 m from the land. Our results support this finding, showing the highest positive MB (RMSE) of 0.58 °C (1.78 °C) by SST_{Lsat} for retrievals closest to the coast (0–90 m) (Figure 6, Table 5). Here, SST_{Lsat} biases were amplified seasonally, overestimating in the spring/summer (0.71 °C) and underestimating in the winter (−1.05 °C), likely as a direct result of land thermal contributions. Interestingly, moving further from the land–water

boundary, the 90–180 m distance group exhibited a negative spring/summer MB (RMSE) of -0.57 °C (1.75 °C) and MRB of -4.13% . At this distance, winter matchups (Figure 7, Table 6) again underestimated nearshore SST (MB of -1.10 °C, MRB -15.84% , and RMSE of 1.55). Beyond land thermal contributions, cold temperature (<15.0 °C) underestimation by Landsat has been reported in the literature [10,12,37,51,52]. At lower temperatures, there is a greater signal-to-noise ratio due to weak target signal strength, causing thermal calibration algorithms to overcompensate for perceived noise interference [10,51]. Similar to the nearshore data, our SST_{Lsat} retrievals from the farshore (where there are no land thermal contributions) showed that winter temperatures (<9.0 °C) were consistently underestimated by almost 1.0 °C (MB of -0.76 °C and MRB -7.39%). As such, further adjustment may be required for using winter SST_{Lsat} retrievals in future applications. At the mid–high dynamic temperature range (10.0 – 25.0 °C), farshore matchups resulted in an average MB of 0.23 °C and MRB 1.23% . Specifically, during the spring/summer, the MB and MRB were 0.12 °C and 0.38% , respectively. These findings indicate a high level of confidence in using SST_{Lsat} retrievals during the spring and summer months in coastal regions of the Northeast Pacific.

Geographically, the nearshore in situ sites included in this analysis covered different levels of exposure to wind/tidal mixing (Table 1), leading to slightly different SST_{Lsat} validation results. For instance, for the spring/summer 90–180 m matchups (Figure 8) from Race Rocks and Entrance Island (Figure 2), which are relatively more exposed coastal locations with high mixing [28], a negative SST_{Lsat} MB of on average -1.23 °C and MRB of $\sim -8.5\%$ were observed. In comparison, at Departure Bay, a significantly less exposed location (Figure 2), a positive SST_{Lsat} MB of 0.67 °C and MRB 4.23% were observed (Table 7). Land adjacency occurs at all sites; however, it may be enhanced in sheltered areas where geographies are more complex (e.g., added contributions from small islets off the coast of the Departure Bay site) [8]. Additionally, local bathymetry may impact the quality of matchups by enhancing the sensitivity of the region to surface warming by insolation and stratification [28]. Therefore, areas that experience less mixing are perhaps more sensitive to matchup uncertainties due to temporal differences compared to exposed sites.

Although we observed small average biases, with 95% confidence intervals between -0.14 °C and 0.19 °C (MB of 0.03 °C) and -0.72 °C and -0.42 °C (MB of -0.57 °C) for the farshore and nearshore environments, respectively, the difference in an individual matchup can be much larger than the population MB. For the farshore, five samples were more than 2 °C different than the $SST_{in situ}$. For the nearshore (Figure 8), 35 samples displayed a difference larger than 3 °C of $SST_{in situ}$. However, the low overall bias observed in the majority of nearshore data (95%) gives confidence in using the Landsat SST retrievals to synoptically characterize temperature trends in coastal waters. However, as with any satellite retrieval, end-users interested in Landsat ARD should use caution when interpreting single SST_{Lsat} measurements rather than averages or larger populations, particularly in the nearshore environment.

5.2. Sources of Uncertainty: Matchup Quality and Characteristics

Other important considerations in the validation of SST_{Lsat} are the quality and characteristics of the in situ data considered. Discrepancies between the depth of water where measurements are taken can lead to differences during validation that are not actually reflective of satellite product accuracy [12,34,41,53,54]. To reduce the impact of depth discrepancies on the matchup analysis, a subsurface-to-skin temperature adjustment was applied to farshore in situ measurements [12,34,37,38]. The results are presented in Supplementary Material Figure S1 and generally altered the $SST_{in situ}$ within 0.2 °C of observed buoy temperatures at a 1 m depth. At the nearshore locations, it is assumed that the “bucket method” [32] retrieves well-mixed surface waters from <1 m depth directly off the local lighthouse dock (pers. comm., [36]). It is likely that the exact depth of sampling may vary over time due to differing personnel, which may have introduced inconsistencies into the BC Lighthouse SST dataset, though the sampling methods themselves have remained

consistent since 1914 [32,36]. Nonetheless, this is our only source of long-term in situ nearshore SST for the Salish Sea.

Furthermore, skin water temperatures measured by Landsat are extremely sensitive to the effects of insolation [12,55]. Insolation, in this context, refers to heating by sun rays, and generally follows a diurnal pattern [12,38]. To limit farshore matchup uncertainty associated with temporal heating differences, buoy SST_{in situ} measurements were selected within 1 h of the noon LST, as close as possible to the satellite overpass. However, there is a time lag between surface heating by insolation and mixing with subsurface waters [34,38]. This depends on the depth of the ocean-mixed layer, which fluctuates seasonally in the Salish Sea [25,56], largely as a function of wind speed [38]. The exclusion of low-wind condition (<1 m/s) matchups [12,38,57] from the farshore analysis reduced errors associated with the intense stratification of surface waters. Additionally, since all matchups occurred within the same day (within +/−6 h), we expected reduced uncertainty associated with diurnal surface heating differences compared to past work by Schaeffer et al. [6], where multiday in situ and satellite matchups were considered to validate the SST from Landsat 5 and 7. Schaeffer et al. [6] reported a mean absolute error (MAE) of 2.40 °C for +/−3-day matchups, and 1.12 °C for +/−1-day matchups [6]. In comparison, for same day (+/−6 h), nearshore 90–180 m, spring/summer matchups, we found an MAE of 1.31 °C.

Across all three lighthouse sites (Figure 8, Table 3), the nearshore SST_{Lsat} from spring/summer at 90–180 m was negatively biased across the entire in situ thermal range (5.6 °C to 22.6 °C), with the largest general underestimation by SST_{Lsat} (MB of −1.84 °C; MRB −8.63%) during the warmest ocean temperatures (>20 °C). This is an unexpected finding compared to the farshore analysis, which experienced general overestimation (0.51 °C; MRB of 2.42%) at the upper range of ocean temperatures (>20 °C). However, these results may be an artifact of the aforementioned depth and temporal differences between matchups rather than intrinsic properties of the Landsat ARD products themselves. During warm water conditions (>20 °C) in the Salish Sea, enhanced heating by insolation in shallow areas directly adjacent to the coast [29], where the SST_{in situ} is sampled, may be poorly captured by the SST_{Lsat} at 90–180 m from the coast, where the water is deeper and greater mixing occurs. Such characteristics of the data could be an important consideration for future studies using Landsat ARD ST products to investigate marine heat waves and other extreme temperature events [18–20].

5.3. Sources of Uncertainties: Sensor-Specific and Calibration Biases

Given the highly dynamic nature of coastal waters in the Northeast Pacific, much of the matchup differences reported here are likely associated with depth and temporal discrepancies [6,37] rather than properties of the Landsat ARD products themselves. However, sensor-specific and thermal product calibration biases also need to be considered. Dwyer et al. [11] provided a comprehensive explanation of Landsat ARD, including calibration methods.

Sensor-specific biases are an especially important consideration for time-series analysis when multiple satellites are included [49]. At the farshore site, Landsat 5, 7, and 8 (Figure 5, Table 1) showed mean biases (RMSE) of −0.28 °C (0.96 °C), 0.10 °C (1.05 °C), and 0.65 °C (0.98 °C), respectively. These results align with the described margins of error for Landsat ARD ST products across satellites [11,12,51] and follow a similar pattern to those reported by the literature in which, generally, Landsat 5 retrievals underestimate and Landsat 8 generally overestimate the SST [10,12,41]. During the development of Landsat ARD products, Cook et al. [12] reported an ARD bias ± standard deviation of −0.52 °C ± 0.72 °C for Landsat 5, −0.24 °C ± 0.81 °C for Landsat 7, and −0.01 °C ± 0.90 °C for Landsat 8 Band 10 retrieval of SST compared to in situ NOAA buoys. Hook et al. [52] reported the negative bias of Landsat 5 as possibly related to changes in the instrument temperature associated with instrument usage. Challenges with Landsat 8 TIRS have been attributed to stray light contamination issues [48,51] and the absolute calibration of thermal data, which can change spatially/temporally [48].

During the vicarious calibration of Landsat thermal bands, uncertainty in observed thermal radiance can be introduced during Level-1 data acquisition [51], which is inherited into Level-2 ARD products. Schott et al. [58] identified uncertainty in predicted thermal radiance due to instrument noise during radiometric calibration. Further down the processing pipeline, uncertainty inherited from auxiliary datasets used to extract ST from Level-1 TOA thermal radiance can further introduce errors. Malakar et al. [10] attributed land ST retrieval uncertainty (RMSE of 1.23 °C over a variety of surface types) with surface emissivity estimates derived from ASTER GED data [12]. However, due to the well-known emissivity and relative homogeneity of water [59], the error introduced from surface emissivity correction is likely far less significant during SST retrieval than land ST retrieval [10]. As such, the MB (RMSE) over inland water bodies was reported by Malakar et al. [10] as -0.2 °C (0.6 °C) and 0.4 °C (0.8 °C) for Landsat 5 and 7, respectively.

Furthermore, Cook et al. [12] attributed the larger bias \pm standard deviation (-0.52 °C \pm 0.72 °C) of Landsat 5 to the atmospheric (water vapour) compensation component of product calibration, which incorporates NARR atmospheric data into the MODTRAN radiative transfer model during the atmospheric correction of Level-1 data. The proximity of clouds to sample locations increases matchup uncertainty [12,60]. For example, the removal of six cloud-contaminated points from a 603-point Landsat 5 matchup dataset by Cook et al. [12] altered the MB \pm RMSE from 0.57 K \pm 0.084 K to -0.52 K \pm 0.72. The effect of clouds to Landsat 7-retrieved ST was also reported by Laraby and Schott [43], where RMSE increased when clouds were <1 km from the sample site (RMSE of 2.61 °C) compared to clouds >40 km away (RMSE of 0.51 °C). Beyond initial image filtering for $<10\%$ cloud cover [12], the stringent flagging of nearby cloud-contaminated image pixels using associated quality assessment (QA) layers is recommended.

Currently, Landsat ARD products are only available for the continental US, Alaska, and Hawaii. Proximity of the study area to the US border allowed for the validation of ARD in Canadian waters. However, global ST coverage is available with Landsat Level-2 Science Products (L2SP), which follow nearly identical data production protocols as ARD (Landsat 4–7: https://d9-wret.s3.us-west-2.amazonaws.com/assets/palladium/production/s3fs-public/media/files/LSDS-1618_Landsat-4-7_C2-L2-ScienceProductGuide-v4.pdf (accessed on 13 February 2022), Landsat 8–9: https://d9-wret.s3.us-west-2.amazonaws.com/assets/palladium/production/s3fs-public/media/files/LSDS-1619_Landsat8-9-Collection2-Level2-Science-Product-Guide-v5.pdf (accessed on 13 February 2022)). The main difference between ARD and L2SP ST products is the use of tile-based versus scene-based organizational systems. Future validation is recommended for L2SP to assess the accuracy of SST retrieval in dynamic coastal regions.

6. Conclusions

Level-2 ARD ST products from Landsat 5, 7, and 8 have proven to be a very reliable source for high-resolution satellite-derived SST for the spring and summer that can provide insights into synoptic temperature conditions of nearshore areas on the west coast of Canada. In this novel study, metrics were tested for the selection of the highest quality nearshore SST_{Lsat} pixels. These methods can be implemented by a wide variety of end-users for large-scale studies (geographically and temporally) with limited additional image processing requirements. Such information is highly valuable to researchers, decision-makers, and local communities for marine habitat monitoring and climate change resiliency planning [5,10,61].

The agreement of the SST_{Lsat} bias with those reported in the literature [6,10,12,41,51] supports the confidence of this analysis and the recommendation of Landsat ARD products for SST retrieval in the Northeast Pacific, given the consideration of a general spring/summer farshore (>10 km) SST_{Lsat} bias (MRB; RMSE) of 0.12 °C (0.38%; 0.95 °C) and a nearshore (90–180 m) SST_{Lsat} bias (MRB; RMSE) of -0.57 °C (-4.13% ; 1.75 °C). Here, nearshore results represent the best sampling distance from the Low Water Mark to minimize uncertainty associated with adjacent land contamination and pixel mixing on satellite SST,

while sampling as close as possible to the critical nearshore habitats of interest [9,18–20]. However, as with any satellite-acquired thermal data, end-users interested in Landsat ARD should use caution when interpreting single SST_{Lsat} measurements rather than averages or larger populations [8,10,11,15], particularly in the nearshore environment, where we observed 35 samples (out of 475) with a difference larger than 3 °C of $SST_{in situ}$.

Sensor-specific calibration uncertainties can be minimized during SST_{Lsat} retrieval by excluding winter or very low-temperature images [12,51] and ensuring that there are no clouds < 1 km of the sample site during satellite overpass [43]. However, varying biases across the sensor—(MB ± RMSE) for Landsat 5 (−0.28 °C ± 0.95 °C), Landsat 7 (0.10 °C ± 1.05 °C), and Landsat 8 (0.65 °C ± 0.98 °C)—may impact time-series analysis of SST trends. Therefore, continued quality assurance of regional SST_{Lsat} accuracy via validation with $SST_{in situ}$ is recommended for future studies [43]. These considerations may also be extended to Landsat L2SP ST products where ARD coverage is unavailable.

Overall, atmospherically and geometrically corrected Landsat ARD products provide thermal data that are accessible to a broad demographic of end-users [11,19,61]. At 30 m resolution, it is able to capture nuanced coastal SST dynamics across vast regions with minimal additional image processing. Such satellite-derived SST can complement traditional in situ sampling and should be considered part of the comprehensive management toolbox in the age of global ocean warming and biodiversity loss.

Supplementary Materials: The following supporting information can be downloaded at: <https://www.mdpi.com/article/10.3390/rs16050920/s1>, Figure S1: (Above) Results for buoy in situ SST adjustment from subsurface water temperature to skin water temperature based on formulas 1 and 2 adapted from Cook et al. [12] and Zeng et al. [38]. (Below) Distribution of subsurface-to-skin temperature adjustment magnitudes.

Author Contributions: A.W., S.S., C.J.N. and M.C. all contributed to the conception of the research. A.W. gathered, processed, and analyzed the data. A.W. wrote the original draft of the manuscript. S.S., C.J.N., M.C. and A.W. all contributed to the editing of the manuscript. All authors have read and agreed to the published version of the manuscript.

Funding: Funds were available from the Natural Sciences and Engineering Research Council of Canada Alliance grant awarded to MC (Ref. number: ALLRP 566735-21).

Data Availability Statement: The data presented in this study are available upon request from the corresponding author (awachmann@uvic.ca). The data are not publicly available due to data storage limitation—no other restrictions exist.

Acknowledgments: Thank you to the University of Victoria and the Spectral Remote Sensing Lab for providing computational facilities for this study. S.S. would like to also thank/acknowledge the Forrest Research Foundation for funding. This research was originally conducted as part of an honours thesis (2022) by A.W. towards a BSc Honours in Geography at the University of Victoria, BC, Canada. Thank you to Alex Guyn for his support during the early stages of the research and initial investigation of the data. Thank you to Lianna Gendall for her advice and mentorship. Thank you to NASA and the USGS for acquiring and providing spaceborne data and Fisheries and Oceans Canada for their in situ monitoring and dissemination of oceanographic data. Special thanks to Andrea Jans Van Rensburg and Connor Dean for their camaraderie during late nights in the Geomatics Lab and GIS troubleshooting.

Conflicts of Interest: The authors declare no conflicts of interest.

References

1. Hollmann, R.; Merchant, C.J.; Saunders, R.; Downy, C.; Buchwitz, M.; Cazenave, A.; Chuvieco, E.; Defourny, P.; de Leeuw, G.; Forsberg, R.; et al. The ESA climate change initiative: Satellite data records for essential climate variables. *Bull. Am. Meteorol. Soc.* **2013**, *94*, 1541–1552. [[CrossRef](#)]
2. Centurioni, L.R.; Turton, J.; Lumpkin, R.; Braasch, L.J.; Brassington, G.B.; Chao, Y.; Charpentier, E.; Chen, Z.; Corlett, G.K.; Dohan, K.; et al. Global in situ observations of essential climate and ocean variables at the air–sea interface. *Front. Mar. Sci.* **2019**, *6*, 419. [[CrossRef](#)]

3. Reynolds, R.W.; Rayner, N.A.; Smith, T.M.; Stokes, D.C.; Wang, W. An improved in situ and satellite SST analysis for climate. *J. Clim.* **2002**, *15*, 1609–1625. [[CrossRef](#)]
4. Chandler, P.C. Long-term temperature and salinity at BC lighthouses. In *State of Physical, Biological, and Selected Fishery Resources of Pacific Canadian Marine Ecosystems*; Fisheries and Oceans Canada: Sidney, BC, Canada, 2010.
5. Minnett, P.; Alvera-Azcárate, A.; Chin, T.; Corlett, G.; Gentemann, C.; Karagali, I.; Li, X.; Marsouin, A.; Marullo, S.; Maturi, E.; et al. Half a century of satellite remote sensing of sea-surface temperature. *Remote Sens. Environ.* **2019**, *233*, 111366. [[CrossRef](#)]
6. Schaeffer, B.A.; Iames, J.; Dwyer, J.; Urquhart, E.; Salls, W.; Rover, J.; Seegers, B. An initial validation of Landsat 5 and 7 derived surface water temperature for US lakes, reservoirs, and estuaries. *Int. J. Remote Sens.* **2018**, *39*, 7789–7805. [[CrossRef](#)]
7. Chandler, P.C. Sea surface temperature and salinity trends observed at lighthouses and weather buoys in British Columbia, 2014. In *State of the Physical, Biological and Selected Fishery Resources of Pacific*; Fisheries and Oceans Canada: Sidney, BC, Canada, 2014.
8. Brewin, R.J.W.; Smale, D.A.; Moore, P.J.; Dall'olmo, G.; Miller, P.I.; Taylor, B.H.; Smyth, T.J.; Fishwick, J.R.; Yang, M. Evaluating operational AVHRR sea surface temperature data at the coastline using benthic temperature loggers. *Remote Sens.* **2018**, *10*, 925. [[CrossRef](#)]
9. Starko, S.; Bailey, L.A.; Creviston, E.; James, K.A.; Warren, A.; Brophy, M.K.; Danasel, A.; Fass, M.P.; Townsend, J.A.; Neufeld, C.J. Environmental heterogeneity mediates scale-dependent declines in kelp diversity on intertidal rocky shores. *PLoS ONE* **2019**, *14*, e0213191. [[CrossRef](#)]
10. Malakar, N.K.; Hulley, G.C.; Hook, S.J.; Laraby, K.; Cook, M.; Schott, J.R. An operational land surface temperature product for Landsat thermal data: Methodology and validation. *IEEE Trans. Geosci. Remote Sens.* **2018**, *56*, 5717–5735. [[CrossRef](#)]
11. Dwyer, J.L.; Roy, D.P.; Sauer, B.; Jenkerson, C.B.; Zhang, H.K.; Lymburner, L. Analysis ready data: Enabling analysis of the Landsat archive. *Remote Sens.* **2018**, *10*, 1363. [[CrossRef](#)]
12. Cook, M.; Schott, J.R.; Mandel, J.; Raqueno, N. Development of an operational calibration methodology for the Landsat thermal data archive and initial testing of the atmospheric compensation component of a Land Surface Temperature (LST) product from the archive. *Remote Sens.* **2014**, *6*, 11244–11266. [[CrossRef](#)]
13. Schroeder, S.B.; Dupont, C.; Boyer, L.; Juanes, F.; Costa, M. Passive remote sensing technology for mapping bull kelp (*Nereocystis luetkeana*): A review of techniques and regional case study. *Glob. Ecol. Conserv.* **2019**, *19*, e00683. [[CrossRef](#)]
14. Feng, L.; Hu, C. Land adjacency effects on MODIS Aqua top-of-atmosphere radiance in the shortwave infrared: S statistical assessment and correction. *J. Geophys. Res. Ocean.* **2017**, *122*, 4802–4818. [[CrossRef](#)]
15. Smale, D.A.; Wernberg, T. Satellite-derived SST data as a proxy for water temperature in nearshore benthic ecology. *Mar. Ecol. Prog. Ser.* **2009**, *387*, 27–37. [[CrossRef](#)]
16. Barnes, R.A.; Holmes, A.W.; Barnes, W.L.; Esaias, W.E.; McClain, C.R.; Svitek, T.; Hooker, S.B.; Firestone, E.R.; Acker, J.G. *Volume 23: Seawifs Prelaunch Radiometric Calibration and Spectral Characterization (No. REPT-94B00144-VOL-23)*; Seawifs Technical Report Series; Goddard Space Flight Center: Greenbelt, MD, USA, 1994.
17. Cavanaugh, K.C.; Bell, T.; Costa, M.; Eddy, N.E.; Gendall, L.; Gleason, M.G.; Hessian-Lewis, M.; Martone, R.; McPherson, M.; Pontier, O.; et al. A Review of the Opportunities and Challenges for Using Remote Sensing for Management of Surface-Canopy Forming Kelps. *Front. Mar. Sci.* **2021**, *8*, 1536. [[CrossRef](#)]
18. Starko, S.; Neufeld, C.J.; Gendall, L.; Timmer, B.; Campbell, L.; Yakimishyn, J.; Druehl, L.; Baum, J.K. Microclimate predicts kelp forest extinction in the face of direct and indirect marine heatwave effects. *Ecol. Appl.* **2022**, *32*, e2673. [[CrossRef](#)] [[PubMed](#)]
19. Gendall, L.; Schroeder, S.B.; Wills, P.; Hessian-Lewis, M.; Costa, M. A Multi-Satellite Mapping Framework for Floating Kelp Forests. *Remote Sens.* **2023**, *15*, 1276. [[CrossRef](#)]
20. Mora-Soto, A.; Schroeder, S.; Gendall, L.; Wachmann, A.; Narayan, G.R.; Read, S.; Pearsall, I.; Rubidge, E.; Lessard, J.; Martell, K.; et al. Kelp dynamics and environmental drivers in the southern Salish Sea. *Front. Mar. Sci.* **2024**, *11*, 1323448. [[CrossRef](#)]
21. Schroeder, S.B.; Boyer, L.; Juanes, F.; Costa, M. Spatial and temporal persistence of nearshore kelp beds on the west coast of British Columbia, Canada using satellite remote sensing. *Remote Sens. Ecol. Conserv.* **2020**, *6*, 327–343. [[CrossRef](#)]
22. Supratya, V.P.; Coleman, L.J.; Martone, P.T. Elevated temperature affects phenotypic plasticity in the bull kelp (*Nereocystis luetkeana*, Phaeophyceae). *J. Phycol.* **2020**, *56*, 1534–1541. [[CrossRef](#)]
23. Iwabuchi, B.L.; Gosselin, L.A. Long-term trends and regional variability in extreme temperature and salinity conditions experienced by coastal marine organisms on Vancouver Island, Canada. *Bull. Mar. Sci.* **2019**, *95*, 337–354. [[CrossRef](#)]
24. Kaldy, J.E. Effect of temperature and nutrient manipulations on eelgrass *Zostera marina* L. from the Pacific Northwest, USA. *J. Exp. Mar. Biol. Ecol.* **2014**, *453*, 108–115. [[CrossRef](#)]
25. Suchy, K.D.; Le Baron, N.; Hilborn, A.; Perry, R.I.; Costa, M. Influence of environmental drivers on spatio-temporal dynamics of satellite-derived chlorophyll-a in the Strait of Georgia. *Prog. Oceanogr.* **2019**, *176*, 102134. [[CrossRef](#)]
26. Crawford, W.R.; Thomson, R.E. Physical oceanography of the western Canadian continental shelf. *Cont. Shelf Res.* **1991**, *11*, 669–683. [[CrossRef](#)]
27. Schiltroth, B.; Bisgrove, S.; Heath, B. Effects of warm ocean temperatures on bull kelp forests in the Salish Sea. In *Salish Sea Ecosystem Conference 2018*; Western Washington University: Bellingham, WA, USA, 2018.
28. Thompson, R.E. Oceanography of the British Columbia coast. *Can. Spec. Publ. Fish. Aquat. Sci.* **1981**, *50*, 291.
29. Khangaonkar, T.; Nugraha, A.; Xu, W.; Balaguru, K. Salish Sea response to global climate change, sea level rise, and future nutrient loads. *J. Geophys. Res. Ocean.* **2019**, *124*, 3876–3904. [[CrossRef](#)]

30. British Columbia Ministry of Environment. *Indicators of Climate Change for British Columbia: 2016 Update*; Ministry of Environment: British Columbia, Canada, 2016.
31. Cummins, P.F.; Masson, D. Climatic variability and trends in the surface waters of coastal British Columbia. *Prog. Oceanogr.* **2014**, *120*, 279–290. [[CrossRef](#)]
32. DFO. British Columbia Lighthouse Sea-Surface Temperature and Salinity Data, 1914-Present. British Columbia Shore Station Oceanographic Program. Department of Fisheries and Oceans Canada. 2021b. Available online: <https://open.canada.ca/data/en/dataset/719955f2-bf8e-44f7-bc26-6bd623e82884> (accessed on 19 November 2021).
33. Smit, A.J.; Roberts, M.; Anderson, R.J.; Dufois, F.; Dudley, S.F.J.; Bornman, T.G.; Olbers, J.; Bolton, J.J. A coastal seawater temperature dataset for biogeographical studies: Large biases between in situ and remotely-sensed data sets around the coast of South Africa. *PLoS ONE* **2013**, *8*, e81944. [[CrossRef](#)]
34. Donlon, C.J.; Minnett, P.J.; Gentemann, C.; Nightingale, T.J.; Barton, I.J.; Ward, B.; Murray, M.J. Toward improved validation of satellite sea surface skin temperature measurements for climate research. *J. Clim.* **2002**, *15*, 353–369. [[CrossRef](#)]
35. DFO. Marine Environmental Data Section Archive. Ecosystem and Oceans Science. Department of Fisheries and Oceans Canada. 2021a. Available online: <https://meds-sdmm.dfo-mpo.gc.ca/> (accessed on 29 November 2021).
36. DFO. Institute of Ocean Sciences Data Archive. Ocean Sciences Division. Department of Fisheries and Oceans Canada. 2022. Available online: <https://www.pac.dfo-mpo.gc.ca/science/oceans/data-donnees/index-eng.html> (accessed on 10 January 2022).
37. Vanhellemont, Q.; Brewin, R.J.; Bresnahan, P.J.; Cyronak, T. Validation of Landsat 8 high resolution Sea Surface Temperature using surfers. *Estuar. Coast. Shelf. Sci.* **2022**, *265*, 107650. [[CrossRef](#)]
38. Zeng, X.; Zhao, M.; Dickinson, R.E.; He, Y. A multiyear hourly sea surface skin temperature data set derived from the TOGA TAO bulk temperature and wind speed over the tropical Pacific. *J. Geophys. Res. Ocean.* **1999**, *104*, 1525–1536. [[CrossRef](#)]
39. Berk, A.; Conforti, P.; Kennett, R.; Perkins, T.; Hawes, F.; Van Den Bosch, J. MODTRAN@6: A major upgrade of the MODTRAN@radiative transfer code. In Proceedings of the 2014 6th Workshop on Hyperspectral Image and Signal Processing: Evolution in Remote Sensing (WHISPERS), Lausanne, Switzerland, 24–27 June 2014; IEEE: New York, NY, USA, 2014; pp. 1–4.
40. Wang, M.; Zhang, Z.; Hu, T.; Liu, X. A practical single-channel algorithm for land surface temperature retrieval: Application to landsat series data. *J. Geophys. Res. Atmos.* **2019**, *124*, 299–316. [[CrossRef](#)]
41. Duan, S.-B.; Li, Z.-L.; Wang, C.; Zhang, S.; Tang, B.-H.; Leng, P.; Gao, M.-F. Land-surface temperature retrieval from Landsat 8 single-channel thermal infrared data in combination with NCEP reanalysis data and ASTER GED product. *Int. J. Remote Sens.* **2019**, *40*, 1763–1778. [[CrossRef](#)]
42. Hossain, M.S.; Bujang, J.S.; Zakaria, M.H.; Hashim, M. Assessment of Landsat 7 Scan Line Corrector-off data gap-filling methods for seagrass distribution mapping. *Int. J. Remote Sens.* **2015**, *36*, 1188–1215. [[CrossRef](#)]
43. Laraby, K.G.; Schott, J.R. Uncertainty estimation method and Landsat 7 global validation for the Landsat surface temperature product. *Remote Sens. Environ.* **2018**, *216*, 472–481. [[CrossRef](#)]
44. Baughman, C.A.; Conaway, J.S. Comparison of Historical Water Temperature Measurements with Landsat Analysis Ready Data Provisional Surface Temperature Estimates for the Yukon River in Alaska. *Remote Sens.* **2021**, *13*, 2394. [[CrossRef](#)]
45. Werdell, P.J.; McKinna, L.I.; Boss, E.; Ackleson, S.G.; Craig, S.E.; Gregg, W.W.; Lee, Z.; Maritorena, S.; Roesler, C.S.; Rousseaux, C.S.; et al. An overview of approaches and challenges for retrieving marine inherent optical properties from ocean color remote sensing. *Prog. Oceanogr.* **2018**, *160*, 186–212. [[CrossRef](#)]
46. Giannini, F.; Hunt, B.P.; Jacoby, D.; Costa, M. Performance of OLCI Sentinel-3A satellite in the Northeast Pacific coastal waters. *Remote Sens. Environ.* **2021**, *256*, 112317. [[CrossRef](#)]
47. Nasiha, H.J.; Wang, Z.; Giannini, F.; Costa, M. Spatial variability of in situ above-water reflectance in coastal dynamic waters: Implications for satellite match-up analysis. *Front. Remote Sens.* **2022**, *3*, 876748. [[CrossRef](#)]
48. Schott, J.R.; Gerace, A.; Raqueno, N.; Ientilucci, E.; Raqueno, R.; Lunsford, A.W. Chasing the TIRS ghosts: Calibrating the Landsat 8 thermal bands. In *Earth Observing Systems XIX*; SPIE: Bellingham, WA, USA, 2014; Volume 9218, pp. 409–428.
49. Qiu, S.; Lin, Y.; Shang, R.; Zhang, J.; Ma, L.; Zhu, Z. Making Landsat time series consistent: Evaluating and improving Landsat analysis ready data. *Remote Sens.* **2019**, *11*, 51. [[CrossRef](#)]
50. Keys, R. Cubic convolution interpolation for digital image processing. *IEEE Trans. Acoust. Speech Signal Process.* **1981**, *29*, 1153–1160. [[CrossRef](#)]
51. Barsi, J.A.; Schott, J.R.; Hook, S.J.; Raqueno, N.G.; Markham, B.L.; Radocinski, R.G. Landsat-8 thermal infrared sensor (TIRS) vicarious radiometric calibration. *Remote Sens.* **2014**, *6*, 11607–11626. [[CrossRef](#)]
52. Hook, S.; Chander, G.; Barsi, J.; Alley, R.; Abtahi, A.; Palluconi, F.; Markham, B.; Richards, R.; Schladow, S.; Helder, D. In-flight validation and recovery of water surface temperature with Landsat-5 thermal infrared data using an automated high-altitude lake validation site at Lake Tahoe. *IEEE Trans. Geosci. Remote Sens.* **2004**, *42*, 2767–2772. [[CrossRef](#)]
53. Casey, K.S.; Cornillon, P. A comparison of satellite and in situ-based sea surface temperature climatologies. *J. Clim.* **1999**, *12*, 1848–1863. [[CrossRef](#)]
54. Robinson, I.S.; Wells, N.C.; Charnock, H. The sea surface thermal boundary layer and its relevance to the measurement of sea surface temperature by airborne and spaceborne radiometers. *Int. J. Remote Sens.* **1984**, *5*, 19–45. [[CrossRef](#)]
55. Kaplan, D.M.; Largier, J.L.; Navarrete, S.; Guíñez, R.; Castilla, J.C. Large diurnal temperature fluctuations in the nearshore water column. *Estuar. Coast. Shelf Sci.* **2003**, *57*, 385–398. [[CrossRef](#)]

56. Kara, A.B.; Rochford, P.A.; Hurlburt, H.E. An optimal definition for ocean mixed layer depth. *J. Geophys. Res. Ocean.* **2000**, *105*, 16803–16821. [[CrossRef](#)]
57. Arafteh-Dalmau, N.; Schoeman, D.S.; Montaña-Moctezuma, G.; Micheli, F.; Rogers-Bennett, L.; Olguin-Jacobson, C.; Possingham, H.P. Marine heat waves threaten kelp forests. *Science* **2020**, *367*, 635. [[CrossRef](#)]
58. Schott, J.R.; Hook, S.J.; Barsi, J.A.; Markham, B.L.; Miller, J.; Padula, F.P.; Raqueno, N.G. Thermal infrared radiometric calibration of the entire Landsat 4, 5, and 7 archive (1982–2010). *Remote Sens. Environ.* **2012**, *122*, 41–49. [[CrossRef](#)]
59. Vanhellemont, Q. Automated water surface temperature retrieval from Landsat 8/TIRS. *Remote Sens. Environ.* **2020**, *237*, 111518. [[CrossRef](#)]
60. Springer, Y.P.; Hays, C.G.; Carr, M.H.; Mackey, M.R. Toward ecosystem-based management of marine macroalgae—the bull kelp, *Nereocystis luetkeana*. *Oceanogr. Mar. Biol.* **2010**, *48*, 1–42.
61. Wulder, M.A.; Loveland, T.R.; Roy, D.P.; Crawford, C.J.; Masek, J.G.; Woodcock, C.E.; Allen, R.G.; Anderson, M.C.; Belward, A.S.; Cohen, W.B.; et al. Current status of Landsat program, science, and applications. *Remote Sens. Environ.* **2019**, *225*, 127–147. [[CrossRef](#)]

Disclaimer/Publisher’s Note: The statements, opinions and data contained in all publications are solely those of the individual author(s) and contributor(s) and not of MDPI and/or the editor(s). MDPI and/or the editor(s) disclaim responsibility for any injury to people or property resulting from any ideas, methods, instructions or products referred to in the content.